PCCP

Plasma Parameters and the Reduction Potential at a Plasma-Liquid Interface

Plasma Parameters and the Reduction Potential at a Plasma-Liquid Interface

Trey Oldham[1], Shurik Yatom[2], and Elijah Thimsen[1,3,a]

[1] Department of Energy, Environmental & Chemical Engineering, Washington University in St. Louis, St. Louis, MO, USA
[2] Princeton Plasma Physics Laboratory, Princeton University, Princeton, NJ, USA
[3] Institute of Materials Science & Engineering, Washington University in St. Louis, St. Louis, MO, USA

[a] **Author to whom correspondence should be addressed:** elijah.thimsen@wustl.edu

Abstract

Nonthermal plasmas in contact with liquids have been shown to generate a variety of reactive species capable of initiating reduction-oxidation (redox) reactions at the electrochemically active plasma-liquid interface. In conventional electrochemical cells, selective redox chemistry is achieved by controlling the reduction potential at the solid electrode-electrolyte interface by applying a bias via an external circuit. In the case of plasma-liquid systems, an analogous means of tuning the reduction potential near the interface has not clearly been identified. When treated as a floating surface, the liquid is expected to adopt a net negative charge to balance the flux of hot electrons and relatively cold positive ions. The reduction potential near the plasma-liquid interface is hypothesized to be proportional to the floating potential, which can be approximated using an analytical model provided the plasma parameters are known. Herein, we present a framework for correlating the electron density and electron temperature of a noble gas plasma jet to the reduction potential near the plasma-liquid interface. The plasma parameters were acquired for an argon atmospheric plasma jet in contact with an aqueous solution by means of laser Thomson scattering. The reduction potential was determined using identical reference electrodes to measure the potential difference between the plasma-liquid interface and bulk solution. Interestingly, the measured reduction potentials near the plasma-liquid interface were found to be in good agreement with the model-predicted values determined using the plasma parameters obtained from the Thomson scattering experiments.

1. Introduction

The increasing availability and decreasing cost of renewable electricity has prompted research into electrified chemical processing whereby electrical energy is used to drive chemical transformations.[1,2] Electricity-intensive processing techniques such as electrochemistry using solid electrodes has attracted attention in this context for the synthesis of organic compounds, such as high-value pharmaceuticals[3] and renewable chemical production.[4] Chemical transformations are achieved in conventional electrolytic electrochemical cells by applying a bias to a solid electrode allowing for the preferential transfer of electrons across the electrode-liquid interface. The ability to perform controlled

reduction-oxidation (redox) reactions in electrolytic systems is realized by adjusting the electrode potential at the electrode-liquid interface via external circuitry (*e.g.* a potentiostat).[5] However, conventional electrolytic cells have been shown to suffer from complications including fouling of the electrode surfaces by carbonaceous coatings[6–8] and reaction selectivity that is dependent on the electrode material.[9,10] Another way to utilize electricity to drive chemical reactions is by employing nonthermal plasma in contact with liquids.

Nonthermal atmospheric plasma interacting with liquids have been utilized for a variety of applications including wastewater treatment,[11–13] chemical conversion,[14–17] and nanomaterial synthesis.[18–21] These applications are based on electrochemical reactions induced by charge-transfer processes taking place across the interface formed between the plasma and electrolyte solution (i.e. plasma-liquid interface). Nonthermal plasma in contact with liquids can act as a source of reactive species such as solvated electrons,[22] atomic hydrogen,[23] and reactive oxygen and nitrogen species (RONS),[24–27] which can facilitate redox reactions within solution. Nonthermal plasma-liquid interactions have been described as a means of performing electrodeless electrochemistry.[28] More recently, nonthermal free atmospheric pressure plasma jets (APPJs) in contact with liquids have been shown to form an electrodeless cathode and anode in the liquid[29] capable of promoting selective organic transformations.[30] Rather than modulating the energy of an electron confined in an electrode using the conventional electrochemistry approach, plasma initiates electrochemical reactions using free electrons. An electrodeless approach is hypothesized to ameliorate issues of electrode fouling experienced using solid electrodes[6–8] as well as electrode material-dependent reactivity.[9,10] Despite these features compared to conventional electrochemical systems, a means of performing controlled chemical transformations on the liquid side of the plasma-liquid interface has not been clearly identified. More specifically, a framework for understanding how the reduction potential in plasma-liquid systems can be tuned for controlled electrochemistry has not been established.

Electrochemical reactions are driven by differences in the electrochemical potential of electrons between dissimilar phases. The difference in electrochemical potential of electrons results in the transfer of electrons across the interface until local equilibrium is reached. The reduction potential, E, was defined by Gerischer[31,32] as

$$E = -\frac{\overline{\mu}_e}{F} \tag{1}$$

where is μ_e is electrochemical potential of electrons (Fermi level) and F is the Faraday constant. The electrochemical potential of electrons is the sum of the chemical potential and electrostatic potential energy,[33] which for a particle with charge number -1 is

$$\overline{\mu}_e = \mu_e^* + R_g T \ln\left(\gamma_e[e]\right) - F\Psi \tag{2}$$

where μ_e^* is the standard state chemical potential of the electrons, which is usually taken at a concentration of 1 mol per liter and temperature T. R_g is the ideal gas constant, T is the absolute

temperature, γ_e is the activity coefficient of the electrons, $[e]$ is the molar concentration of electrons, and Ψ is the electrostatic potential. In the case of conventional aqueous electrolytic systems, an external bias is applied to a working electrode to modulate the local electrode potential at the electrode-liquid interface to a particular value, thereby driving redox reaction in solution towards local equilibrium with that reduction potential. We hypothesize an analogous constraint to occur in plasma-liquid systems, wherein the local reduction potential in the liquid immediately underneath the plasma-liquid interface is controlled by the state variables of the plasma (i.e. electron density and electron temperature) above the interface.

In this work, we investigate the effect that the electron density and electron temperature have on the observed reduction potential directly underneath the plasma-liquid interface. The electron density, n_e, and electron temperature, T_e, were measured by means of laser Thomson scattering on a radiofrequency (RF) argon (Ar) APPJ. The reduction potential for a plasma electrochemistry system cannot be measured using the same approach as conventional electrochemistry, since it would contain a contribution from the high applied voltage required to generate the plasma. Instead, characterization of the reduction potential in solution was performed using a previously reported technique,[29,30] where a reference electrode is used to measure the local potential within the solution directly underneath the electrochemically active plasma-liquid interface, E_{PLI}, relative to the potential measured by a nominally identical reference electrode in the bulk solution, E_{inf}. Using this method, one measures the potential driving electrochemical reactions. The relative reduction potential in solution near the plasma-liquid interface, η_{PLI}, is given by

$$\eta_{PLI} = E_{PLI} - E_{inf} . \tag{3}$$

Similar to the reduction potential measured in conventional electrochemical configurations, more positive and more negative values of η_{PLI} are indicative of oxidation and reduction, respectively.[29] The magnitude of η_{PLI} has also been shown to be related to the rate of reaction,[30] which is also the case in conventional systems. Assuming local equilibrium within the liquid, the measured voltage η_{PLI} is equal to the difference in the reduction potential in solution between the reference electrodes. Taking any temperature difference between the two reference electrodes to be negligible, any contribution from the standard state chemical potential μ_e^* introduced in Equation 2 will cancel out. Thus, the difference between the reduction potential in the two locations is caused by differences in the molar concentration of electrons, activity coefficient, and electrostatic potential energy.

Treating the liquid as an electrically floating surface, a negative charge would be expected to form in order to balance the flux of hot electrons and relatively slow positive ions from the plasma phase to the liquid.[34,35] Thus, the constraining potential at the plasma-liquid interface is expected to be proportional to the floating potential, which can be approximated using an analytical model if n_e and T_e are known. Interestingly, the empirical values of the relative reduction potential near the plasma-liquid

interface, η_{PLI}, were found to be in good agreement with the model-predicted reduction potential determined using the plasma parameters obtained from the Thomson scattering experiments.

2. Experimental

The plasma source studied in this work was an RF (13.56 MHz) Ar APPJ shown in Fig. 1. The APPJ was comprised of a powered nickel needle electrode with an outer diameter of 2.3 mm housed within an alumina tube with inner and outer diameters of 3.2 mm and 9.5 mm, respectively. The ground electrode was an aluminum ring with an inner diameter of 9.5 mm, which was mounted to the exterior of the alumina tube at a distance of 5 mm from the tube outlet. The Ar flow rate was maintained at a constant flow rate of 1000 standard cubic centimeters per minute (sccm) using a mass flow controller (GE50A, MKS Instruments). The plasma was generated using a RF power supply (AG 0613, T&C Power Conversion) connected to an impedance matching network (AIT-600 RF Auto Tuner, T&C Power Conversion) and synchronized to the laser source using a pulse generator (Model 575 Pulse/Delay Generator, Berkeley Nucleonics Corporation). The RF excitation frequency was modulated with a 20 kHz pulse with a duty cycle of 20% (i.e., plasma is turned on for 10 μs and off for 40 μs).

Characterization of the Ar APPJ used in this work was accomplished by means of laser light scattering. All laser diagnostics reported in this work were performed in the Princeton Collaborative Research Facility at the Princeton Plasma Physics Laboratory. The laser source for the light scattering experiments was a frequency-doubled Nd:YAG laser (λ_0 = 532 nm, Continuum SL-III, Surelite). The laser was Q-switched at a repetition rate of 10 Hz, generating a beam with a pulse width of 8 ns (full width at half max, FWHM) and a maximum pulse energy of 550 mJ. A schematic for the experimental apparatus used for the laser scattering experiments is shown in Fig. 2. The incident laser was focused with a lens (focal distance f = 1 m) and the laser spot size interacting with the plasma was determined to be 318 μm in diameter. The laser pulse energy used in the experiments was monitored using a pyroelectric energy sensor (ES220C, ThorLabs) and was set to be 60 mJ. The operating laser fluence used for Raman and Thomson scattering was 75.6 J cm^{-2}, which was found to be less than the critical fluence that would result in inverse bremsstrahlung heating of electrons (Electronic Supplementary Information, ESI, Note 1). The orientation of the detection arm was orthogonal (ϕ = 90°) to the axis of the incident laser. Light scattered by the plasma was focused (f = 200 mm) through a 200 μm pinhole, which acted as a spatial filter. A volume Bragg notch filter (BNF) was used to physically remove the Rayleigh component of the scattered light. The filter was a reflecting volume Bragg grating (VBG) and was specified to block light with an optical density of 4 with a FWHM of 5-8 cm^{-1} (0.14-0.23 nm). The transmission of the filter outside the blocking region is 80%. The reflected wavelength can be tuned by rotating the filter. Setting an angle of 6° between the filter normal and the direction of the incoming light results in the reflection of 532 nm light, which is the central wavelength (λ_0) of the laser. The main drawback of the VBG filter is the small angular acceptance of less than 0.1°, therefore, adequate collimation of the scattered light is crucial for rejecting Rayleigh scattered light. Light exiting the

pinhole was collimated (f = 50 mm) before passing the volume Bragg notch filter, and focused (f = 50 mm) into the entrance slit of the monochromator (SpectraPro HRS-750, Princeton Instruments) and projected onto an intensified CCD (iCCD) camera (Pi-Max 3 Model 1024i, Princeton Instruments). Irises were placed along the detection arm in order to minimize stray light due to light scattering from solid surfaces. The iCCD captures a two-dimensional image with the spectral dispersion (wavelength) along the horizontal axis and spatial information along vertical axis (ESI, Fig. S2 in Note 2). The iCCD images of the collected scattered light were averaged over 10000 accumulations (17 minutes) for each spectrum. A digital pulse/delay generator was used to synchronize the laser, RF power supply, and iCCD camera.

Laser light scattering was performed on an Ar APPJ treating a 75 μM indigo carmine (IC) solution with an adjusted pH of 10. The solution was contained in a 325 mL PTFE crystallizing dish, which produced a positive meniscus to minimize any stray light from the dish. The PTFE dish was connected to a large reservoir containing 14 L of freshly prepared 75 μM IC solution (pH 10) in order to maintain a constant liquid height in the PTFE dish via hydrostatic pressure while the Thomson signal was being acquired. The plasma was positioned such that the end of the tube was at a fixed height of 10 mm above the surface of the solution, with the laser passing through the plasma at a height of 8 mm above the liquid surface (see inset of Fig. 2). Thomson signal was acquired as a function of RF power over the range of 20-50 W, increasing the power in increments of 10 W. Prior to each Thomson experiment, the solution in the PTFE dish was replenished with fresh solution from the reservoir. An alignment procedure for centering the plasma jet along both the laser and detection axes was performed before each acquisition. The plasma jet was mounted to a two-axis micrometer positioning table, allowing for the relative position of the plasma jet to be adjusted in 25.4 μm increments along the laser and detection axes. Alignment of the plasma along the laser axis was based on locating the core of the plasma by means of Rayleigh scattering. To that end the angle of the BNF was changed to allow the Raleigh scattering (RS) through to the detector. The position of the plasma along the laser axis was then adjusted to minimize the RS signal, which corresponds to the position with the lowest density of heavy particles due to highest temperature. We assume that the hottest region corresponds to the highest electron density (i.e. e-n collisions are the dominant gas heating mechanism). Along the detection arm, alignment of the plasma with the entrance slit of the spectrometer was determined based on the position with the strongest H_α (653.6 nm) and/or broadband light emission which were found to coincide.

Electrochemical characterization was carried out using a previously reported method,[30] based on measuring the potential difference between a position within the liquid near the plasma-liquid interface (E_{PLI}) and the bulk solution (E_{inf}). Briefly, the relative reduction potential was measured using identical Ag/AgCl reference electrodes connected to a digital multimeter (DMM6500, Keithley). The reference electrode measuring the relative reduction potential of the electrochemically active plasma-liquid interface was housed in a Luggin capillary (Adams & Chittenden) and positioned in the liquid directly underneath the impingement point of the plasma. In a recent work,[29] we observed that the

measured magnitude of the reduction potential dissipates with depth below the surface, thus the Luggin capillary was submerged at an approximate depth of 0.2 mm below the solution surface to prevent any distortion due to surface tension while minimizing any apparent drop off in magnitude. The Luggin capillary was aligned with the end of the APPJ tube to ensure the measurement was centered below the plasma-liquid interface to measure the potential at the electrodeless cathode, which was verified after igniting the plasma. The local reduction potential within the liquid underneath the plasma-liquid interface was referenced to the potential measured by an identical reference electrode positioned in the unaffected bulk solution and time-averaged over a 45 second duration. The relative reduction potential measurements were performed as a function of RF power in the same PTFE dish using in the Thomson scattering experiments using 75 μM IC (pH 10). The reduction reaction of IC occurs by a two proton, two electron transfer as given by

$$(4)$$
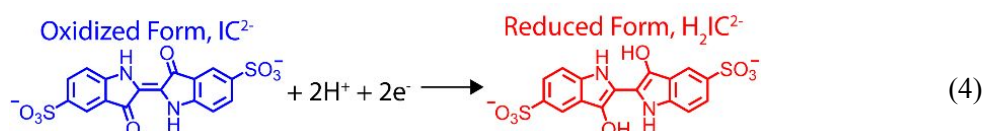
The measured voltage difference between the electrodes prior to igniting the plasma was used for baseline subtraction. However, due to the stringent nature of the Thomson scattering experiments, the electrochemical measurements were performed asynchronously to avoid the introduction of additional stray light. In order to verify that the Ar APPJ used in this work was able to selectively reduce the model redox compound (e.g. IC), the composition of the solution was treated at the same RF powers used in the Thomson scattering experiments and evaluated using ultraviolet-visible absorption spectroscopy (ESI, Note 3).

3. DATA ANALYSIS & FITTING

3.1. Laser Light Scattering

More detailed explanations regarding the theory behind light scattering of plasmas can be found elsewhere,[36–38] but a brief overview will be discussed. Light guided through a plasma can be scattered as a result of interactions between the incident electromagnetic radiation and heavy particles (Rayleigh scattering), molecules (Raman scattering), or unbound charged particles (Thomson scattering). Rayleigh scattering arises from elastic scattering of light by the electron clouds (i.e. bound electrons) of atoms and molecules.[36,39] Raman scattering describes the inelastic scattering of light with the bound electrons of molecules, which induce rotational and/or vibrational transitions.[40,41] Thomson scattering occurs as a result of elastic scattering of light from unbound charges (e.g. electrons or ions).[36,41,42] In the context of plasma laser diagnostics, analysis of the resulting light scattering spectrum for a given mechanism is key for extracting a characteristic density and/or temperature. Rayleigh scattering can be used to determine the background gas temperature (T_g), Raman scattering can provide the densities of

molecular species (e.g. N_2 and O_2) and the rotational temperature (T_{rot}), and Thomson scattering can be used to extract the electron density (n_e) and electron temperature (T_e).[43]

The general form of the power of scattered light per unit wavelength, $P_\lambda(\lambda)$, for each scattering mechanism is expressed as[36,37]

$$P_\lambda(\lambda) = fLP_0\Delta\Omega \cdot n_i \cdot \frac{d\sigma_i}{d\Omega} \cdot S_i(\lambda) \tag{5}$$

where f is based on the efficiency of the optics and camera, L is the length of the detection arm, P_0 is the power of the incident laser, $\Delta\Omega$ is the solid angle of detection, n_i is the number density of species i, $\frac{d\sigma_i}{d\Omega}$ is the differential cross section of species i, and $S_i(\lambda)$ is function that describes the spectral distribution of scattered photons. While n_i, $\frac{d\sigma_i}{d\Omega}$, and $S_i(\lambda)$ are unique to the type of light scattering, $fLP_0\Delta\Omega$ is a system-specific geometrical factor that has a constant value for a particular apparatus and setup and does not depend on the scattering mechanism. Given that the profile of $S_i(\lambda)$ takes on a specific form based on the type of light scattering, along with the fact that $\frac{d\sigma_i}{d\Omega}$ is typically a known quantity, the value of $fLP_0\Delta\Omega$ can be readily determined by performing light scattering under known conditions (*i.e.* species density and temperature) by a procedure known as absolute intensity calibration. More specifically, an experimental scattering spectrum, $P_{exp}(\lambda)$, and a simulated spectrum calculated using Equation 4 can be used to find the intensity calibration factor by

$$fLP_0\Delta\Omega = \frac{P_{exp}(\lambda)}{n_i \cdot \frac{d\sigma_i}{d\Omega} \cdot S_i(\lambda)}. \tag{6}$$

For APPJs, the calibration factor is typically found by means of performing rotational Raman scattering under ambient conditions in open air. In the case of Thomson scattering, the $fLP_0\Delta\Omega$ factor is typically required to accurately determine the n_e.

Thomson scattering can be categorized as being collective or non-collective depending on the relative scales of the incident laser wavelength, λ_0, and the electron Debye length, λ_D, given by

$$\lambda_D = \left(\frac{\varepsilon_0 k_B T_e}{q_e^2 n_e}\right)^{1/2}. \tag{7}$$

where ε_0 is the permittivity of free space, k_B is the Boltzmann constant, and q_e is the fundamental charge. More specifically, the scattering regime is determined by the value of the scattering parameter, α, expressed as

$$\alpha = \frac{1}{2\sqrt{2}\pi} \cdot \frac{\lambda_0}{\lambda_D} \tag{8}$$

which describes the degree of collectivity. Note that the first term on the right-hand side of Equation 8 only applies for systems in which the scattering angle $\phi = 90°$ is orthogonal to the incident laser. Non-

collective Thomson scattering occurs for $\lambda_0 = \lambda_D$ ($\alpha < 1$), where the incident light is scattered by individual electrons. Collective scattering takes place when $\lambda_0 ? \lambda_D$ ($\alpha > 1$), where light is scattered by an ensemble (i.e. a collection) of electrons.

The spectral shape in a Thomson scattering experiment is a consequence of Doppler shifting of light due to the relative motion (velocity) of electrons with respect to both the incident laser beam and the detector. Thus, the resulting scattering spectrum is related to the velocity distribution of the electrons in the plasma. For non-collective Thomson scattering (*i.e.* $\lambda_0 = \lambda_D$), the randomly distributed electrons within the plasma result in the isotropic scattering of light. Assuming that the electron velocity distribution is Maxwellian, the observed Thomson spectrum would take on a Gaussian profile with a width proportional to T_e and an area proportional to n_e. It should be noted that the area is also dependent on $fLP_0\Delta\Omega$, as shown in Equation 5, highlighting the importance of proper calibration when determining n_e. For collective Thomson scattering (*i.e.* $\lambda_0 ? \lambda_D$), light interactions with groups of electrons result in nonuniform scattering, introducing wave interference effects. While the underlying Maxwellian velocity distribution of electrons profile is still present, the spectral distribution function is modified to account for collective effects using the scattering parameter, α

$$S_e(x_e) = \frac{1}{\sqrt{\pi}} \cdot \frac{\exp(-x_e^2)}{\left|1 + \alpha^2 W(x_e)\right|^2} \tag{9}$$

where x_e is a dimensionless parameter and $W(x_e)$ is the plasma dispersion function. The value of x_e is given by

$$x_e = \frac{c\lambda_0}{\sqrt{2}} \cdot \left(\frac{1}{\lambda} - \frac{1}{\lambda_0}\right) \cdot \left(\frac{2k_B T_e}{m_e}\right)^{-1/2} \tag{10}$$

where c is the speed of light in a vacuum. The complex plasma dispersion function is expressed as

$$W(x_e) = 1 - 2x_e e^{-x_e^2} \int_0^{x_e} e^{t^2} dt - j\sqrt{\pi} x_e e^{-x_e^2} \tag{11}$$

where t is a dummy variable and j is an imaginary unit. The spectral distribution function, given by Equation 9, takes on a unique shape based on the value of α (ESI, Fig. S4 in Note 4). A noticeable deviation from the Gaussian spectral shape becomes apparent for $\alpha \geq 0.2$, giving rise to a partially collective scattering regime. The distinct shape of the Thomson signal in the partially collective and collective scattering regimes allow for n_e and T_e to be determined without the absolute intensity calibration procedure. Rather, a shape calibration approach can be used, whereby α and T_e are used to adjust the shape and width of $S_e(x_e)$, respectively, to fit the unique shape of the Thomson signal (ESI, Note 4).

3.2. Fitting Procedure

In this work, both absolute intensity calibration and the shape calibration approaches were implemented to fit the Thomson signal. Note that the absolute intensity calibration is used to account for system specific factors including the efficiency of the optics and camera, length of the detection arm, the power of the incident laser, and the solid angle of detection. As such, performing the calibration using the same optical components and experimental conditions as the Thomson scattering experiments is crucial. For the absolute intensity calibration, the Raman signal was first acquired by flowing argon gas (1000 sccm) in open air with no discharge under known atmospheric conditions (i.e. pressure and temperature). The experimental Raman spectrum was fitted only considering rotational transitions N_2 and O_2, following the procedure described by Penney et al.[44], Van de Sande,[37] and van Gessel et al.[43] The rotational temperature (T_{rot}) and mole fractions of nitrogen (x_{N_2}) and oxygen (x_{O_2}) were used as the parameters to fit a simulated Raman spectrum to the experimentally obtained Raman signal in order to determine the system-specific $fLP_0\Delta\Omega$ calibration factor. The absolute intensity calibration approach used the calibration factor to rescale the intensity of the simulated Thomson spectra in order to fit the experimental signal. In the case of the shape calibration approach, the unique shape of the Thomson signal in the collective scattering regime allows for the determination of the plasma parameters without the need of $fLP_0\Delta\Omega$. Instead, the experimental signal can be normalized to eliminate the $fLP_0\Delta\Omega$-dependence directly fitted using the simulated Thomson spectrum.

The fitting procedure used for the absolute intensity and shape calibration of Thomson signal was adapted from the work of Obrusnik et al.[45] For both calibration approaches, a two-step procedure was implemented to fit the experimental Thomson signal using the MATLAB fminsearch and nlinfit functions following the procedure of van Gessel et. al.[43] While the fminsearch function shows good convergence when calculating the least square difference between the fitted and experimental curves, the algorithm does not provide error estimates for the fitted parameters. Conversely, the nlinfit function provides a covariant matrix that can be used for error analysis, but the convergence of the Levenberg-Marquardt nonlinear least squares algorithm is sensitive to the initial values of the fitting parameters. Thus, the fminsearch function was used to determine the initial fit values for α and T_e, which were used as inputs for the nlinfit function to provide error estimates.

3.3. Floating Potential Calculation

The floating potential of a collisional plasma can be correlated to the plasma parameters using an exponential-accuracy model under the assumption that the ion-atom collision frequency is independent of velocity and the ion mobility, μ_+, is constant.[46,47] The floating potential is given by

$$V_f = -\frac{2}{3}\frac{k_B T_e}{q_e}\ln\frac{\Delta}{\lambda_D} - 1.0082\frac{k_B T_e}{q_e} \tag{12}$$

where Δ is the ionization length. The ionization length can be written as

$$\Delta = \frac{n_e k_B T_e \mu_+}{j_+}$$

(13)

where j_+ is the ion current density. The ion current density was approximated using the Child-Langmuir law given by[48]

$$j_+ = \frac{4}{9} \varepsilon_0 \left(\frac{2q_e}{M_+} \right) \frac{V^{3/2}}{d^2}$$

(14)

where M_+ is the ion mass, V is the voltage applied to the electrode, and d is the interelectrode spacing. The applied voltage, V, for each applied RF power was approximated using the root-mean-square of the measured peak voltages (ESI, Fig. S5 in Note 5).

4. Results and Discussion

To understand the relationship between the measured reduction potential in solution, η_{PLI}, and the state variables of the plasma, the plasma parameters were first extracted from the laser light scattering signal. More specifically, the values of n_e and T_e were determined by calibrating and fitting the spectra obtained in the Thomson scattering experiments. The fitted Raman spectrum used for absolute intensity calibration is shown in Fig. 3a. The fitted Raman spectrum (Fig. 3a) showed that T_{rot} = 295 K, which was in agreement with the measured ambient temperature. The mole fractions of nitrogen, $x_{N_2} = 0.805$, and oxygen, $x_{O_2} = 0.195$, obtained from the fit were consistent with the expected composition of ambient air under standard conditions. The experimental Raman signal was normalized in order to determine the system-specific $fLP_0\Delta\Omega$ factor required for absolute intensity calibration used in the Thomson scattering experiments.

The Thomson signal acquired for the Ar APPJ used in this work was found to fall within the collective scattering regime, as observed from the non-Gaussian profile shown in Figs. 3b-c. Although a temporal evolution in the plasma parameters was observed over the course the 10 μs duty cycle, the values of n_e and T_e were found to plateau and remain relatively unchanged approximately 4 μs after the pulse onset, which is discussed in detail in an accompanying publication by Yatom et al.[49] Taking this into account, the plasma parameters reported herein are based on the value within the plateau time period (ESI, Fig. S6 in Note 7), which are representative of the average values of n_e and T_e over the 10 μs pulse. While absolute intensity calibration is not required for determining n_e and T_e in this scattering regime, it can be useful for comparing the results from shape calibration fitting. For the Thomson spectrum acquired for the Ar APPJ operating at 50 W (Fig. 3b), the fitted values for the electron density and temperature using the absolute intensity calibration method were found to $n_e = (7.76 \pm 0.30) \cdot 10^{21}$ m^{-3} and $k_B T_e = 0.90 \pm 0.06$ eV, respectively. Similarly, the shape calibration method was applied to the same data set (Fig. 3c), which showed that the fitted values of $n_e = (7.76 \pm 0.28) \cdot 10^{21}$ m^{-3} and $k_B T_e = 0.90 \pm 0.05$ eV. Note that Raman contribution to the Thomson signal was found to be negligible and omitted from the fit. The absence of Raman features in the Thomson signal is consistent with the idea

that the amount of air entrainment into the flow would be negligible close to the tube ending of the APPJ. Given the close agreement between fitted values for the plasma parameters between both calibration methods, the reported plasma parameters reported herein were calculated based on the shape calibration method.

The Thomson signal was acquired for the Ar APPJ as a function of applied RF power over the range of 20 to 50 W in increments of 10 W. The plasma parameters obtained from fitting the Thomson signal are presented in graphical form in Fig. 4 and tabular form in Table 1. A clear trend was observed in the case of the electron density, which was revealed to increase with increasing applied RF power as shown in Fig. 4. The electron temperature was generally found to increase with increasing power, apart from the 20 and 30 W cases where the values of $k_B T_e$ were determined to be approximately equal. Due to the fact that n_e and $k_B T_e$ both showed similar trends as a function of applied power, the ability to delineate the individual effects that n_e and T_e have on the reduction potential on the liquid side of the plasma-liquid interface becomes difficult.

As an aside, it would be useful to note that the reported plasma parameters were acquired with the laser beam passing through the plasma at a height of 8 mm above the liquid. While attempts at performing the light scattering experiments closer to the plasma-liquid interface were made, dynamic factors of the plasma played a more significant role. In particular, movement in the spatial position of the plasma became more apparent as the laser was moved closer to the liquid surface. The random movements of the plasma became drastic enough to be noticeable by eye and prevented proper laser alignment along both the laser and detection axes. As such, a height of 8 mm above the liquid was chosen in order to minimize the movement of the plasma with respect to the laser beam. Here, we are assuming that the plasma is homogeneous throughout the length of the plasma channel, with negligible variations in the plasma parameters along the axial direction. This is consistent with the reported spatial profiles of the electron density and electron temperature in other atmospheric pressure plasma jets, which showed significant variations near the edges of the plasma while the plasma parameters remained relatively constant close to the core of the plasma jets.[43,50]

A method is needed to describe the reduction potential in solution as a function of both the electron density and the electron temperature. Given that electrochemical interfaces are typically described in terms of potential differences and charge densities, a more suitable framework for relating the plasma parameters to the reduction potential would be based on the potential and charge formation at the plasma-liquid interface.

If the electrolyte solution is conceptualized to be a floating target, a negative surface charge would be expected to form due to the initial flux imbalance between the fast electrons and relatively slow positive ions. At steady state, the net negative charge on the liquid surface results in a potential barrier that repels electrons with insufficient kinetic energy from reaching the surface while attracting slow positive ions to balance the fluxes of electrons and positive ions. For a point charge approaching the interface from either side, the plasma-liquid interface can be approximated as an infinite sheet of

11

charge with an areal charge density of σ, as illustrated in Fig. 5. The point charge experiences a uniform electric field and the potential in each phase can be correlated by

$$\sigma = \frac{\varphi_{\text{plasma}}}{d_{\text{plasma}}} = \frac{\varphi_{\text{liq}}}{d_{\text{liq}}} \tag{15}$$

where φ_i is the potential at a distance d_i from the plasma-liquid interface in phase i. As a positive charge is moved towards the plasma-liquid interface from a point infinitely far away, a potential difference between the unscreened test charge and the interface develops at closer distances to the surface. On the plasma side of the interface, the distance at which screening occurs is given by the electron Debye length (i.e. $d_{\text{plasma}} = \lambda_D$) where the unscreened potential can be approximated using the floating potential (i.e. $\varphi_{\text{plasma}} = V_f$). Here, the floating potential refers to the steady state potential formed to maintain the flux balance between electrons and positive ions. In the liquid, the distance at which screening occurs is given by the electrolyte Debye length ($d_{\text{liq}} = \mathsf{l}_D$) which is expressed as

$$\mathsf{l}_D = \left(\frac{\varepsilon_r \varepsilon_0 k_B T}{N_A q_e^2 \sum_i \left(c_i \cdot 10^3 \right) z_i^2} \right)^{1/2} \tag{16}$$

where ε_r is the relative permittivity, T is the temperature of the solution, N_A is the Avogadro constant, c_i is the molar concentration of ionic species i, and z_i is the charge number of ionic species i. Taking the unscreened potential in the liquid at a distance l_D from the interface to be the relative reduction potential between the plasma-liquid interface and bulk solution, $\varphi_{\text{liq}} = \eta_{\text{PLI}}$, the potentials on both sides of the plasma-liquid interface can be related by

$$\eta_{\text{PLI}} = V_f \cdot \frac{\mathsf{l}_D}{\lambda_D}. \tag{17}$$

In this analysis, changes in the relative reduction potential are caused by differences in the electrochemical potential of electrons in the solution.

The plasma parameters determined from the Thomson scattering experiments were used as inputs for calculating the floating potential as a function of applied RF power using Equations 12-14. The ion mobility and mass used for argon were $1.54 \cdot 10^{-4}$ m^2 V^{-1} s^{-1} and $6.63 \cdot 10^{-26}$ kg, respectively.[51] The electrolyte Debye length was calculated using Equation 16 and found to be $\mathsf{l}_D = 23.0$ nm for the IC solution used in this work. Similarly, the electron Debye lengths were determined with Equation 4 for each electron density and electron temperature listed in Table 1, which ranged from $\lambda_D = 91.2$ nm to 80.1 nm as the applied RF power was increased from 20 to 50 W, respectively. Noting that the contact area of the plasma on the liquid surface is circular with a diameter of approximately 3.6 mm, the charged surface is more than 10^4 times larger than the characteristic screening (Debye) lengths in either the plasma or liquid phase. Thus, the plasma-liquid interface presents itself as effectively an infinite sheet of charges to the vast majority of incoming charged particles approaching from either side. The model predicted value for the relative reduction potential at the plasma-liquid interface, η, was found for each

applied RF power using Equation 17. The results of the time-averaged electrochemical measurements and the model-predicted relative reduction potentials are plotted as a function of RF power as shown in Fig. 6b. Note that the timescale between consecutive time points in the electrochemical measurements was on the order of 10 ms, while the timescale of the RF cycle was on the order of 10 ns. Given the differences in magnitudes, the relative reduction potential measurements are representative of a time-averaged steady state where the net current to the liquid is zero (i.e. the surface is floating) and the polarity of individual RF half-cycles are negligible. The error bars for the experimentally measured relative reduction potential are the standard deviation from time-averaged electrochemical measurements, while the error bars for the modeled-predicted reduction potentials are propagated from the error estimates for the Thomson fit parameters (ESI, Note 6).

As shown in Fig. 6b, the model-predicted reduction potential was found to be in good agreement with the experimentally measured reduction potential. The error bars from the time-averaged reduction potential measurements overlap with the error bars propagated from the model-predicted reduction potential (ESI, Note 6) with the exception of the 50 W case. As discussed in a previous work,[29] the magnitude of η_{PLI} decreases with increasing depth below the plasma-liquid interface. The decreased magnitude of η_{PLI} was attributed to the measurement becoming less representative of the electrochemically active PLI and increasingly representative of the bulk solution with increasing depth. To account for the fact that the measurement was performed 0.2 mm beneath the surface, an extrapolated value for η_{PLI} at the plasma-liquid interface (*i.e.* 0 mm below the surface) was determined based on the previous study. The extrapolated values were also found to agree with the model-predicted reduction potentials and appeared to determine an upper bound for the reduction potential, as shown in Fig. 6b. The disparity between the measured and model-predicted reduction potentials is likely due to simplifying assumptions of the model. In particular, the plasma was assumed to be homogenous throughout the entire length of the channel, with negligible variations in the plasma parameters along the axial direction. While the spatial profiles of the electron density and electron temperature in other atmospheric pressure plasma jets do not show significant variations near the core of the plasma, a subtle decrease in n_e and increase in $k_B T_e$ was noted in the edges of the plasma.[43,50] This would likely improve the accuracy of the model-predicted reduction potential as the electron Debye length would increase with the subtle changes in the downstream plasma parameters, thereby making η less negative. As an independent means of validating the model, an additional supplementary experiment was performed using a helium APPJ (ESI, Fig. S7 in Note 8). The reduction potential was measured for different salt concentrations, and therefore different electrolyte Debye lengths l_D, but identical plasma generation conditions were used (electrode geometry, applied RF power, and gas flow rate). This supplemental independent experiment demonstrated two key points: (1) that the model could describe the scaling in the reduction potential as a function of electrolyte Debye length and (2) that the model was applicable

to noble gas plasmas other than argon, where the gas composition dependence in the floating potential arises in the μ_+ term in Equation 13 and the M_+ term in Equation 14.

5. Conclusions

Laser Thomson scattering was performed on an APPJ in contact with an electrolyte solution, containing a model redox compound, to measure n_e and T_e in the plasma as a function of RF power. Evaluation of the plasma parameters obtained from fitting the experimental Thomson signal using both absolute intensity calibration and shape calibration methods were in excellent agreement. Using a collision-dominated model for calculating the floating potential based on the experimentally measured plasma parameters, a simplistic model for predicting the reduction potential on the liquid side of the plasma-liquid interface was developed. Interestingly, the measured values of the reduction potential were found to be in close agreement with a scaled version of the plasma floating potential. In particular, the scaling factor was found to be the ratio of the electrolyte Debye length to the electron Debye length in the plasma. The ability to understand how the reduction potential at the plasma-liquid interface is related to the plasma parameters is an important first step in understanding how to perform controlled redox reactions using electrodeless plasma-liquid systems. More specifically, this framework provides guidance on how to utilize plasma-liquid systems for promoting selective electrochemistry without the use of solid electrodes.

Conflicts of Interest

There are no conflicts to declare.

ORCiD

Trey Oldham: 0000-0002-4058-1490

Shurik Yatom: 0000-0001-8716-8487

Elijah Thimsen: 0000-0002-7619-0926

Electronic Supplementary Information (ESI)

Laser heating, Raman and Thomson iCCD images, UV-Vis absorption spectra of IC, shape fitting of Thomson signal, voltage waveforms, floating potential error analysis, temporal evolution of plasma parameters, and effect varying electrolyte Debye length.
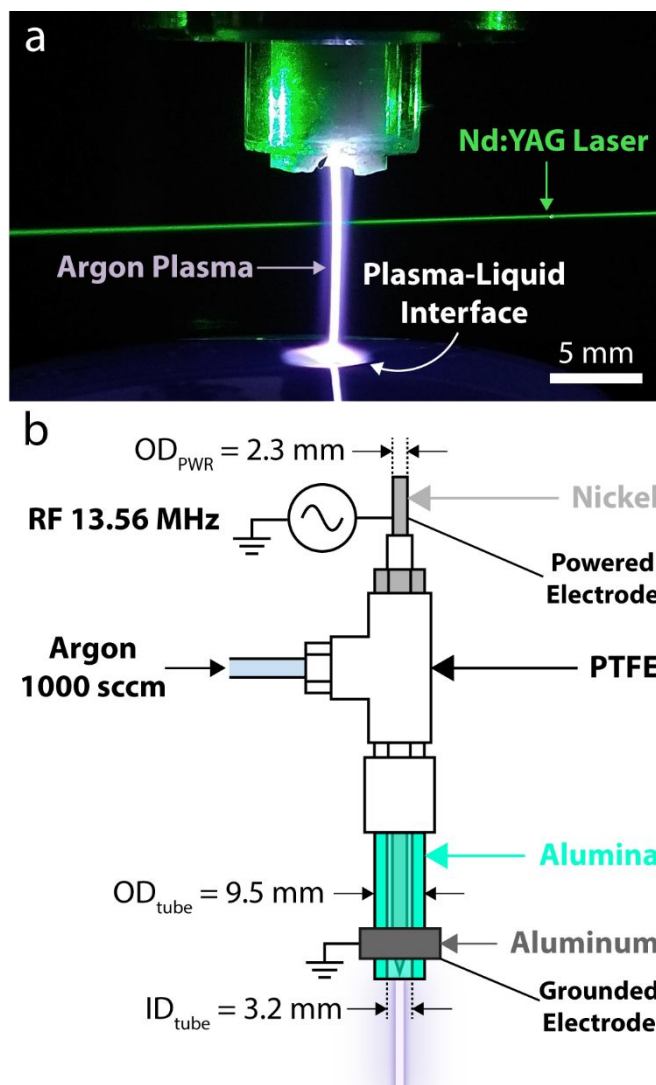
Fig. 1. Laser Thomson scattering from a radiofrequency argon plasma jet. (a) Image of a frequency-doubled Nd:YAG laser passing through core of radiofrequency (RF, 13.56 MHz) argon plasma jet in contact with liquid. The RF excitation frequency was modulated with a 20 kHz pulse with a duty cycle of 20%. (b) Schematic representation of RF argon plasma jet shown in (a) with important dimensions specified.
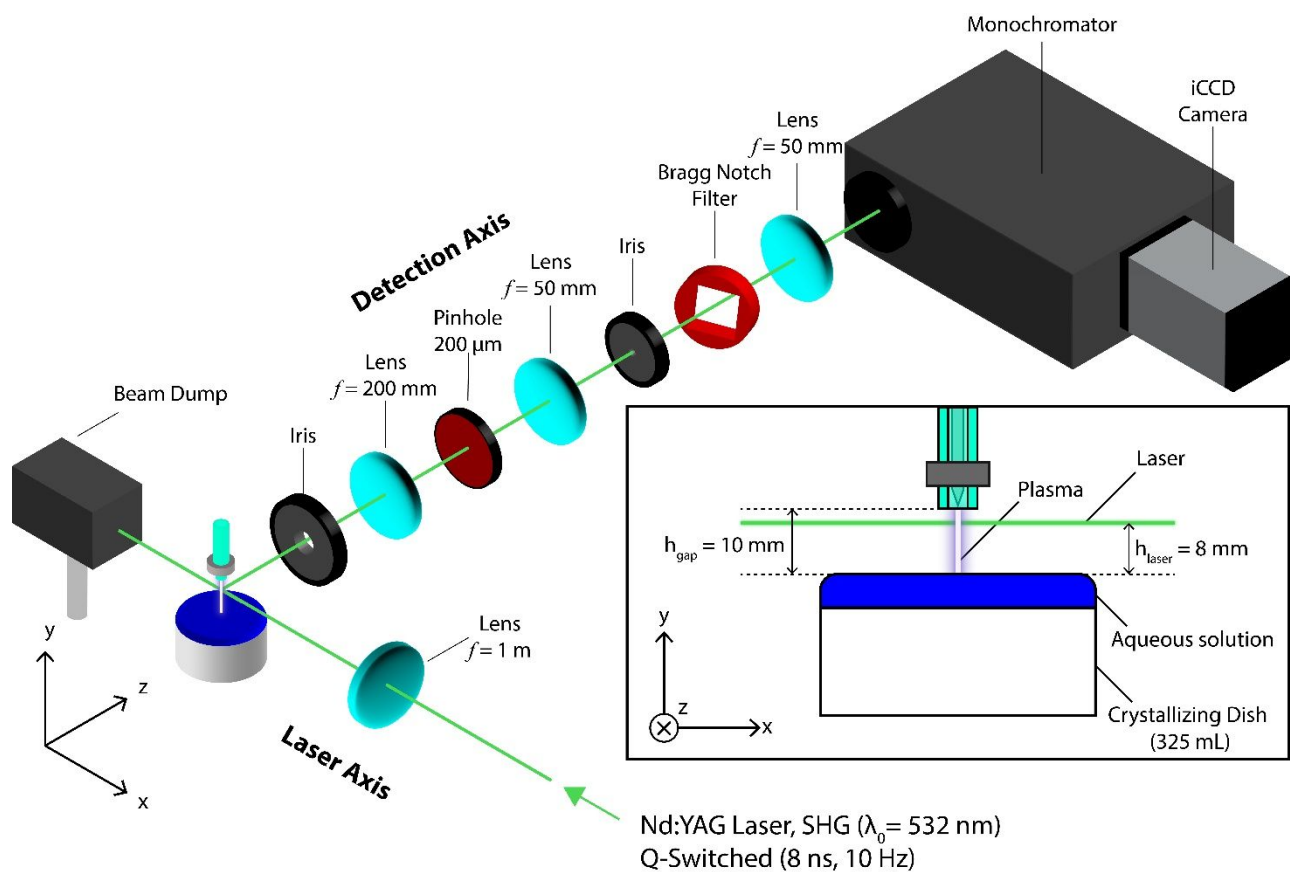
Fig. 2. Schematic of the experimental laser light scattering setup. Laser source used in Raman and Thomson scattering experiments. A Q-switched frequency-doubled Nd:YAG laser was used to generate a beam with a central wavelength of 532 nm at a repetition rate of 10 Hz. The pulse width of the laser was 8 ns and the laser power used for acquiring Thomson signal was 60 mJ. Incident light is focused through a lens (f = 1m) and passed through the plasma at a distance of 2 mm below the APPJ tube ending, or 8 mm above the liquid surface (see inset). The scattered light was collected along the detection arm which was orthogonal to the incident beam. The scattered signal was focused (f = 200 mm) through a pinhole and collimated (f = 50 mm) through a Bragg notch filter to remove the Rayleigh component of the scattered light. The light was focused (f = 50 mm) before entering the monochromator and images were acquired using an intensified CCD (iCCD) camera.
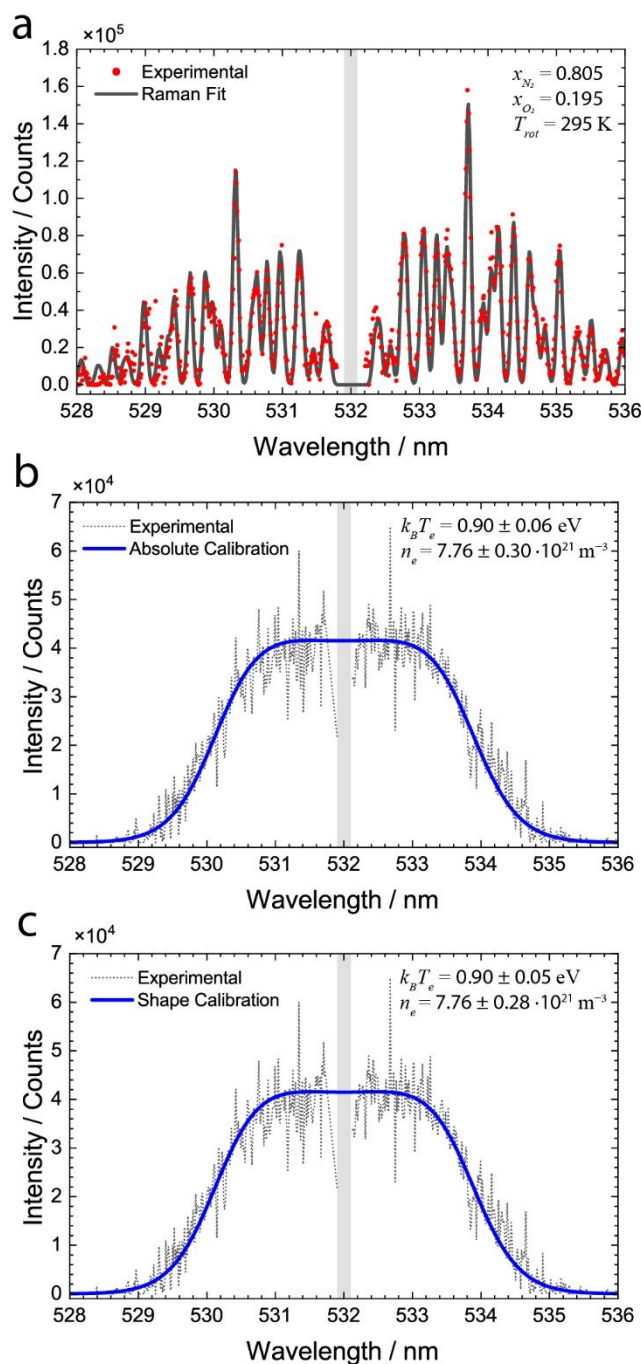
Fig. 3. Raman and Thomson spectra. (a) Experimental Raman spectrum acquired under ambient conditions in open air and fitted rotational Raman spectrum. (b) Experimental Thomson spectrum acquired for argon plasma operating at 50 W with a flow rate of 1000 sccm and fitted spectrum using the absolute intensity calibration method. (c) Same experimental Thomson spectrum from (b) with fitted spectrum based on shape calibration method. Thomson signal shown in (b) and (c) acquired using a laser time delay of 8.881 μs. Fitted parameters for each spectrum are indicated on the top right. Grayed out areas are the Rayleigh rejection region. All spectra were acquired over an accumulation of 10000 laser shots.
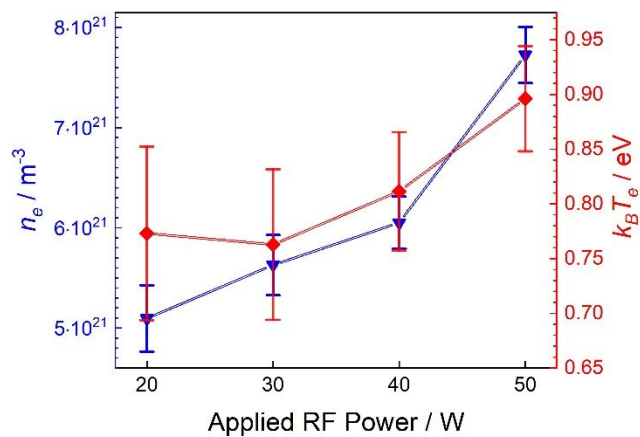
Fig. 4. Electron density and electron temperature as a function of applied RF power. The electron density (blue triangles) and electron temperatures (red diamonds) determined from shape calibration fitting of the experimental laser Thomson signal as a function of applied RF power. Error bars are the error estimates of the Matlab nlinfit function.

Table 1. Summary of plasma parameters. Summarized results of the electron density and electron temperature as a function of applied RF power plotted in Fig. 4. The parameters were obtained using the shape calibration fitting method of the Thomson signal acquired at each RF power indicated. Error determined from the error estimates of the Matlab nlinfit function.

Applied RF Power / W	$k_B T_e$ / eV	n_e ($\cdot 10^{21}$) / m^{-3}
20	0.77 ± 0.08	5.09 ± 0.33
30	0.76 ± 0.07	5.63 ± 0.30
40	0.81 ± 0.05	6.05 ± 0.26
50	0.90 ± 0.05	7.72 ± 0.28
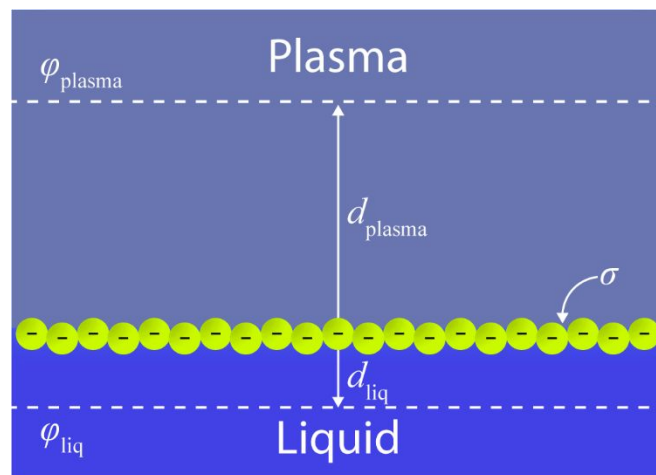
Fig. 5. Schematic Representation of the charged plasma-liquid interface. Illustration depicting the areal charge density formed at the plasma-liquid interface and the unscreened potentials at characteristic lengths for each phase.
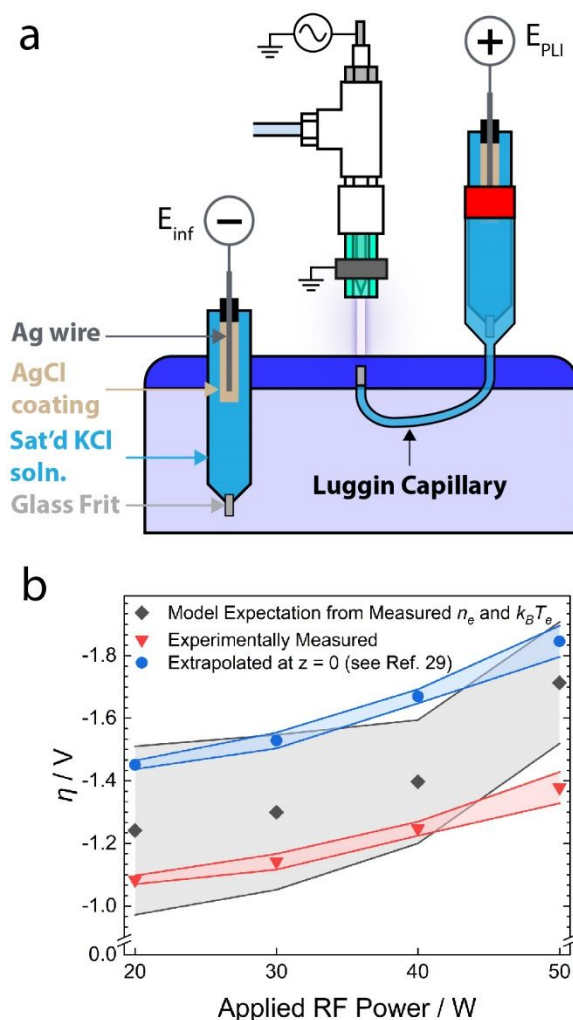
Fig. 6. Experimentally measured reduction potential and model predicted potential as a function of RF power. (a) Schematic representation of Ar APPJ and Ag/AgCl reference electrode measuring local potential within the liquid near the plasma-liquid interface (E_{PLI}) with respect to an identical Ag/AgCl measuring potential in the bulk solution (E_{inf}). The E_{PLI} reference electrode was housed in a Luggin capillary which was positioned directly underneath the stagnation point of the plasma jet. (b) Time-averaged relative reduction potential (red triangles) measured between the plasma-liquid interface and bulk solution. Extrapolated values at z = 0 mm (blue circles) based on results from Ref 29. Error bars are the standard deviation of time-averaged measurements. Model-predicted reduction potential (dark grey diamond) based on floating potential calculated using experimental plasma parameters (see Table 1) from laser Thomson scattering with error bars propagated from the error estimates of the fitted parameters.

References

1 N. M. Haegel, H. Atwater, T. Barnes, C. Breyer, A. Burrell, Y.-M. Chiang, S. D. Wolf, B. Dimmler, D. Feldman, S. Glunz, J. C. Goldschmidt, D. Hochschild, R. Inzunza, I. Kaizuka, B. Kroposki, S. Kurtz, S. Leu, R. Margolis, K. Matsubara, A. Metz, W. K. Metzger, M. Morjaria, S. Niki, S. Nowak, I. M. Peters, S. Philipps, T. Reindl, A. Richter, D. Rose, K. Sakurai, R. Schlatmann, M. Shikano, W. Sinke, R. Sinton, B. J. Stanbery, M. Topic, W. Tumas, Y. Ueda, J. van de Lagemaat, P. Verlinden, M. Vetter, E. Warren, M. Werner, M. Yamaguchi and A. W. Bett, Terawatt-scale photovoltaics: Transform global energy, *Science*, 2019, **364**, 836–838.

2 M. T. Spitler, M. A. Modestino, T. G. Deutsch, C. X. Xiang, J. R. Durrant, D. V. Esposito, S. Haussener, S. Maldonado, I. D. Sharp, B. A. Parkinson, D. S. Ginley, F. A. Houle, T. Hannappel, N. R. Neale, D. G. Nocera and P. C. McIntyre, Practical challenges in the development of photoelectrochemical solar fuels production, *Sustainable Energy Fuels*, 2020, **4**, 985–995.

3 B. K. Peters, K. X. Rodriguez, S. H. Reisberg, S. B. Beil, D. P. Hickey, Y. Kawamata, M. Collins, J. Starr, L. Chen, S. Udyavara, K. Klunder, T. J. Gorey, S. L. Anderson, M. Neurock, S. D. Minteer and P. S. Baran, Scalable and safe synthetic organic electroreduction inspired by Li-ion battery chemistry, *Science*, 2019, **363**, 838–845.

4 I. Bosque, G. Magallanes, M. Rigoulet, M. D. Kärkäs and C. R. J. Stephenson, Redox Catalysis Facilitates Lignin Depolymerization, *ACS Cent. Sci.*, 2017, **3**, 621–628.

5 A. W. Colburn, K. J. Levey, D. O'Hare and J. V. Macpherson, Lifting the lid on the potentiostat: a beginner's guide to understanding electrochemical circuitry and practical operation, *Phys. Chem. Chem. Phys.*, 2021, **23**, 8100–8117.

6 J. Iniesta, Electrochemical oxidation of phenol at boron-doped diamond electrode, *Electrochimica Acta*, 2001, **46**, 3573–3578.

7 M. Panizza and G. Cerisola, Direct And Mediated Anodic Oxidation of Organic Pollutants, *Chem. Rev.*, 2009, **109**, 6541–6569.

8 Y. Feng, L. Yang, J. Liu and B. E. Logan, Electrochemical technologies for wastewater treatment and resource reclamation, *Environ. Sci.: Water Res. Technol.*, 2016, **2**, 800–831.

9 A. M. Couper, D. Pletcher and F. C. Walsh, Electrode materials for electrosynthesis, *Chem. Rev.*, 1990, **90**, 837–865.

10 D. M. Heard and A. J. J. Lennox, Electrode Materials in Modern Organic Electrochemistry, *Angewandte Chemie*, 2020, **132**, 19026–19044.

11 V. Scholtz, J. Pazlarova, H. Souskova, J. Khun and J. Julak, Nonthermal plasma — A tool for decontamination and disinfection, *Biotechnology Advances*, 2015, **33**, 1108–1119.

12 G. R. Stratton, F. Dai, C. L. Bellona, T. M. Holsen, E. R. V. Dickenson and S. Mededovic Thagard, Plasma-Based Water Treatment: Efficient Transformation of Perfluoroalkyl Substances in Prepared Solutions and Contaminated Groundwater, *Environ. Sci. Technol.*, 2017, **51**, 1643–1648.

13 S. Horikoshi and N. Serpone, In-liquid plasma: a novel tool in the fabrication of nanomaterials and in the treatment of wastewaters, *RSC Adv.*, 2017, **7**, 47196–47218.

14 R. Hawtof, S. Ghosh, E. Guarr, C. Xu, R. Mohan Sankaran and J. N. Renner, Catalyst-free, highly selective synthesis of ammonia from nitrogen and water by a plasma electrolytic system, *Science Advances*, **5**, eaat5778.

15 P. Rumbach, R. Xu and D. B. Go, Electrochemical Production of Oxalate and Formate from CO2 by Solvated Electrons Produced Using an Atmospheric-Pressure Plasma, *J. Electrochem. Soc.*, 2016, **163**, F1157.

16 C. Pattyn, N. Maira, A. Remy, N. C. Roy, S. Iseni, D. Petitjean and F. Reniers, Potential of N2/O2 atmospheric pressure needle-water DC microplasmas for nitrogen fixation: nitrite-free synthesis of nitrates, *Phys. Chem. Chem. Phys.*, 2020, **22**, 24801–24812.

17 Z. Wang, C. Xu, Y. Lu, G. Wei, G. Ye, T. Sun and J. Chen, Microplasma-assisted rapid, chemical oxidant-free and controllable polymerization of dopamine for surface modification, *Polymer Chemistry*, 2017, **8**, 4388–4392.

18 P. Galář, J. Khun, A. Fučíková, K. Dohnalová, T. Popelář, I. Matulková, J. Valenta, V. Scholtz and K. Kůsová, Non-thermal pulsed plasma activated water: environmentally friendly way for efficient surface modification of semiconductor nanoparticles, *Green Chem.*, 2021, **23**, 898–911.

19 D. B. Padmanaban, R. McGlynn, E. Byrne, T. Velusamy, M. Swadźba-Kwaśny, P. Maguire and D. Mariotti, Understanding plasma–ethanol non-equilibrium electrochemistry during the synthesis of metal oxide quantum dots, *Green Chem.*, 2021, **23**, 3983–3995.

20 X. Li, L. Lin, W.-H. Chiang, K. Chang and H. Xu, Microplasma synthesized gold nanoparticles for surface enhanced Raman spectroscopic detection of methylene blue, *React. Chem. Eng.*, , DOI:10.1039/D1RE00446H.

21 Z. Wang, Y. Lu, H. Yuan, Z. Ren, C. Xu and J. Chen, Microplasma-assisted rapid synthesis of luminescent nitrogen-doped carbon dots and their application in pH sensing and uranium detection, *Nanoscale*, 2015, **7**, 20743–20748.

22 P. Rumbach, D. M. Bartels, R. M. Sankaran and D. B. Go, The solvation of electrons by an atmospheric-pressure plasma, *Nat Commun*, 2015, **6**, 1–7.

23 V. S. S. K. Kondeti, U. Gangal, S. Yatom and P. J. Bruggeman, Ag+ reduction and silver nanoparticle synthesis at the plasma–liquid interface by an RF driven atmospheric pressure plasma jet: Mechanisms and the effect of surfactant, *Journal of Vacuum Science & Technology A*, 2017, **35**, 061302.

24 F. Girard, M. Peret, N. Dumont, V. Badets, S. Blanc, K. Gazeli, C. Noël, T. Belmonte, L. Marlin, J.-P. Cambus, G. Simon, N. Sojic, B. Held, S. Arbault and F. Clément, Correlations between gaseous and liquid phase chemistries induced by cold atmospheric plasmas in a physiological buffer, *Phys. Chem. Chem. Phys.*, 2018, **20**, 9198–9210.

25 J. Benedikt, M. Mokhtar Hefny, A. Shaw, B. R. Buckley, F. Iza, S. Schäkermann and J. E. Bandow, The fate of plasma-generated oxygen atoms in aqueous solutions: non-equilibrium atmospheric pressure plasmas as an efficient source of atomic O $_{(aq)}$, *Phys. Chem. Chem. Phys.*, 2018, **20**, 12037–12042.

26 C. C. W. Verlackt, W. V. Boxem and A. Bogaerts, Transport and accumulation of plasma generated species in aqueous solution, *Phys. Chem. Chem. Phys.*, 2018, **20**, 6845–6859.

27 P. Heirman, W. V. Boxem and A. Bogaerts, Reactivity and stability of plasma-generated oxygen and nitrogen species in buffered water solution: a computational study, *Phys. Chem. Chem. Phys.*, 2019, **21**, 12881–12894.

28 P. J. Bruggeman, R. R. Frontiera, U. R. Kortshagen, M. J. Kushner, S. Linic, G. C. Schatz, H. Andaraarachchi, S. Exarhos, L. O. Jones, C. M. Mueller, C. C. Rich, C. Xu, Y. Yue and Y. Zhang, Plasma-driven solution electrolysis, *Journal of Applied Physics*, 2021, **129**, 200902.

29 T. Oldham and E. Thimsen, Electrochemical Structure of the Plasma–Liquid Interface, *J. Phys. Chem. C*, 2022, **126**, 1222–1229.

30 T. Oldham, M. Chen, S. Sharkey, K. M. Parker and E. Thimsen, Electrochemical characterization of the plasma-water interface, *J. Phys. D: Appl. Phys.*, 2020, **53**, 165202.

31 H. Gerischer, *Physical Chemistry. An Advanced Treatise. Volume IXA: Electrochemistry*, Academic Press, New York, 1970.

32 H. Gerischer and W. Ekardt, Fermi levels in electrolytes and the absolute scale of redox potentials, *Appl. Phys. Lett.*, 1983, **43**, 393–395.

33 K. A. Dill and S. Bromberg, *Molecular driving forces: statistical thermodynamics in biology, chemistry, physics, and nanoscience*, Garland Science, London ; New York, 2nd ed., 2011.

34 I. P. Raǐzer, *Gas discharge physics*, Springer, Berlin; New York, 1997.

35 A. Bouchoule, Ed., *Dusty plasmas: physics, chemistry, and technological impacts in plasma processing*, Wiley, Chichester ; New York, 1999.

36 H. Kempkens and J. Uhlenbusch, Scattering diagnostics of low-temperature plasmas (Rayleigh scattering, Thomson scattering, CARS), *Plasma Sources Sci. Technol.*, 2000, **9**, 492–506.

37 M. van de Sande and M. J. van de Sande, *Laser scattering on low temperature plasmas: high resolution and stray light rejection*, Technische Universiteit Eindhoven, Eindhoven, 2002.

38 J. Sheffield, Ed., *Plasma scattering of electromagnetic radiation: experiment, theory and computation*, Elsevier, Amsterdam ; Boston, 1st ed., 2011.

39 K. A. Marshall and G. M. Hieftje, Measurement of true gas kinetic temperatures in an inductively coupled plasma by laser-light scattering. Plenary lecture, *J. Anal. At. Spectrom.*, 1987, **2**, 567–571.

40 G. Vaughan, D. P. Wareing, S. J. Pepler, L. Thomas and V. Mitev, Atmospheric temperature measurements made by rotational Raman scattering, *Appl. Opt., AO*, 1993, **32**, 2758–2764.

41 S. G. Belostotskiy, Q. Wang, V. M. Donnelly, D. J. Economou and N. Sadeghi, Three-dimensional gas temperature measurements in atmospheric pressure microdischarges using Raman scattering, *Appl. Phys. Lett.*, 2006, **89**, 251503.

42 J. M. Palomares, E. Iordanova, E. M. van Veldhuizen, L. Baede, A. Gamero, A. Sola and J. J. A. M. van der Mullen, Thomson scattering on argon surfatron plasmas at intermediate pressures: Axial profiles of the electron temperature and electron density, *Spectrochimica Acta Part B: Atomic Spectroscopy*, 2010, **65**, 225–233.

43 A. F. H. van Gessel, E. A. D. Carbone, P. J. Bruggeman and J. J. A. M. van der Mullen, Laser scattering on an atmospheric pressure plasma jet: disentangling Rayleigh, Raman and Thomson scattering, *Plasma Sources Sci. Technol.*, 2012, **21**, 015003.

44 C. M. Penney, R. L. St. Peters and M. Lapp, Absolute rotational Raman cross sections for N2, O2, and CO2, *J. Opt. Soc. Am.*, 1974, **64**, 712.

45 A. Obrusník, P. Synek, S. Hübner, J. J. A. M. van der Mullen, L. Zajíčková and S. Nijdam, Coherent and incoherent Thomson scattering on an argon/hydrogen microwave plasma torch with transient behaviour, *Plasma Sources Sci. Technol.*, 2016, **25**, 055018.

46 M. S. Benilov and S. Coulombe, Modeling a collision-dominated space-charge sheath in high-pressure arc discharges, *Physics of Plasmas*, 2001, **8**, 4227–4233.

47 M. S. Benilov, The Child–Langmuir law and analytical theory of collisionless to collision-dominated sheaths, *Plasma Sources Sci. Technol.*, 2009, **18**, 014005.

48 I. Langmuir, The Effect of Space Charge and Residual Gases on Thermionic Currents in High Vacuum, *Phys. Rev.*, 1913, **2**, 450–486.

49 S. Yatom, T. Oldham and E. Thimsen, Characterization of plasma in RF jet interacting with water: Thomson scattering versus Spectral line broadening, *Plasma Sources Sci. Technol.*, , , DOI:10.1088/1361-6595/ac56ed.

50 C. Jiang, J. Miles, J. Hornef, C. Carter and S. Adams, Electron densities and temperatures of an atmospheric-pressure nanosecond pulsed helium plasma jet in air, *Plasma Sources Sci. Technol.*, 2019, **28**, 085009.

51 H. J. Oskam and V. R. Mittelstadt, Ion Mobilities in Helium, Neon, and Argon, *Phys. Rev.*, 1963, **132**, 1435–1444.